Hydraulic flow through a channel contraction: Multiple steady states

Benjamin Akers[1,a] and Onno Bokhove[2,b]
[1]*Department of Mathematics, University of Wisconsin-Madison, 480 Lincoln Drive, Madison, Wisconsin 53706-1388, USA*
[2]*Department of Applied Mathematics and Institute of Mechanics, Processes and Control Twente, University of Twente, 7500 AE Enschede, The Netherlands*

(Received 3 November 2007; accepted 26 February 2008; published online 1 May 2008)

We have investigated shallow water flows through a channel with a contraction by experimental and theoretical means. The horizontal channel consists of a sluice gate and an upstream channel of constant width b_0 ending in a linear contraction of minimum width b_c. Experimentally, we observe upstream steady and moving bores/shocks, and oblique waves in the contraction, as single and multiple (steady) states, as well as a steady reservoir with a complex hydraulic jump in the contraction occurring in a small section of the b_c/b_0 and Froude number parameter plane. One-dimensional hydraulic theory provides a comprehensive leading-order approximation, in which a turbulent frictional parametrization is used to achieve quantitative agreement. An analytical and numerical analysis is given for two-dimensional supercritical shallow water flows. It shows that the one-dimensional hydraulic analysis for inviscid flows away from hydraulic jumps holds surprisingly well, even though the two-dimensional oblique hydraulic jump patterns can show large variations across the contraction channel. © *2008 American Institute of Physics*. [DOI: 10.1063/1.2909659]

I. INTRODUCTION

We will consider shallow water flows through a contraction, experimentally, analytically, and numerically. In shallow flows in natural or man-made channels, a contraction geometry is not uncommon. It consists of a more or less uniform channel followed by a contraction of the channel into a nozzle where the width is minimal before the channel suddenly or gradually fans out again. Large variations in water flow discharges through such contracting channels may lead to dramatic changes in the flow state, including stowage effects with upstream moving surges. Such phenomena do occur when rivers overflow and the water is funneled underneath constricting bridges or through ravines. More benign flows with one or two oblique hydraulic jumps occur for smaller discharges, e.g., at underpasses for roadside streams [Fig. 1(a)] or through gates of the Dutch Oosterschelde storm surge barrier [Fig. 1(b)]. Similar situations also occur in downslope water-laden debris flows when oversaturated mountain slopes collapse, for example. In this paper, however, we limit ourselves to study the states of water flow through an idealized experimental setup with a uniform channel and linear contraction as an archetype for the abovementioned more complex flow geometries.

More specifically, this work is inspired by two recent papers in (granular) hydraulics. First, Vreman *et al.*[1] investigate the hydraulic behavior of dry granular matter on an inclined chute with a linear contraction. They observe upstream (moving) bores or shocks, a deep reservoir with a structure akin to a Mach stem in the contraction, and oblique hydraulic jumps or shocks in the contraction for one value of the Froude number and increasing values of the scaled nozzle width B_c. The latter is defined by the ratio of the upstream channel width b_0 and nozzle width b_c. (We denote hydraulic jumps as steady "shocks" and bores as shocks interchangeably.) The inclination of the chute was chosen such that the average interparticle and particle wall forces matched the downstream force of gravity to yield a uniform flow in the absence of a contraction. Shallow granular flows are often assumed to be incompressible and modeled with the depth-averaged shallow water equations and a medium-specific, combined theoretically and experimentally, determined friction law.[2–4] It is therefore of interest to contrast these "hydraulic" results for granular flows with those for water flows. Second, Baines and Whitehead[5] considered flows over an obstacle uniform across the channel and up an inclined plane in a uniform channel. By using one-dimensional (1D) hydraulic theory, they found a third steady state besides the upstream (moving) shocks and sub- or supercritical flows and considered its stability. This also motivated us to investigate 1D shallow water flow through a linearly contracting channel. The most intriguing experimental flow regime we found consists of three stable coexisting steady states for certain Froude numbers F_0 and contraction widths B_c. Here, F_0 is the upstream Froude number based on the constant depth just downstream of the sluice gate and the steady-state water discharge. Two of these states, the upstream (moving) bores and supercritical flows (with weak oblique waves), are well known.[6–8] In addition, we find a stable reservoir state with a jump structure akin to a Mach stem in gas dynamics[7,8] in the contraction. It is similar in nature to the intermediate state found for flow over an obstacle within the context of a 1D averaged hydraulic approach used in Ref. 5. However, it is different in that the observed turbulent laboratory flow is three dimensional in our case with a distinct depth-averaged two-dimensional

[a]Electronic mail: akers@math.wisc.edu.
[b]Electronic mail: o.bokhove@math.utwente.nl.

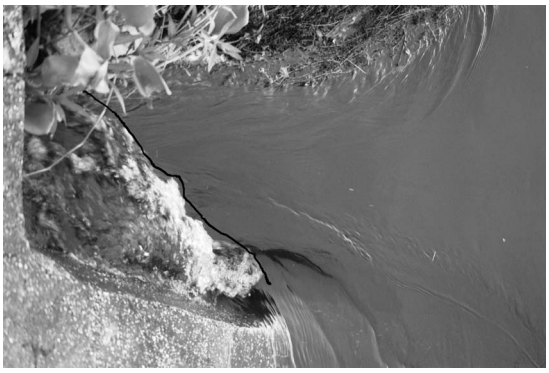

(a)

(b)

FIG. 1. Examples of (a) one oblique hydraulic jump in a roadside stream flowing into an underpass (picture courtesy of V. Zwart), top view and flow from right to left, and (b) two oblique hydraulic jumps in the tidal flow rushing out of one of the sluices in the Oosterschelde storm surge barrier in The Netherlands, side view and flow from left to right. Black lines indicate the hydraulic jumps.

(2D) flow pattern, while the intermediate three-dimensional state in Ref. 5 has a depth-averaged nearly 1D flow pattern.

Nevertheless, 1D hydraulic theory provides a comprehensive albeit approximate overview of the (observed) flow states. It is based on cross sectionally averaging of the flow equations while using hydrostatic balance and including turbulent friction. We first present this approximate theory extending the general classical hydraulic approach in Ref. 6 applied to our specific frictional case in Sec. II.

Subsequently, we introduce the experimental setup and results in Sec. III and identify the differences with the 1D hydraulic theory. Particular attention is paid to the regime with coexisting states and the stable reservoir state with a "Mach stem." However, 1D theory only provides an approximate description of the supercritical oblique waves and the reservoir state.

2D horizontal effects are therefore investigated in Sec. IV. We consider the shallow water equations (semi)analytically for supercritical flows and numerically through some probing simulations for 2D flows inviscid away from the shocks. Hence, we aim to validate 1D hydraulic theory. In addition, we set these calculations by using approximate frictional behavior against laboratory experiments with oblique waves in the contraction. Finally, we conclude and present a last experiment concerning the reservoir regime with the three states in Sec. V.

II. MULTIPLE STEADY STATES IN SHALLOW WATER FLOWS: 1D THEORY

In this section, approximate 1D hydraulic analysis is employed to obtain an overview of the flow states observed in the laboratory. We therefore average the flow quantities over the cross section of a channel slowly varying in width. Fluctuations of the mean are ignored except in a very crude turbulent parametrization because we anticipate large Reynolds numbers in the experimental results that will be presented later. The hydraulic analysis includes this turbulent friction in extension of the inviscid analysis by Refs. 5 and 9–12. Higher order nonhydrostatic effects are largely neglected as well, where the order is determined by the aspect ratio between vertical and downstream scales. The nonhydrostatic three-dimensional turbulence in breaking surface waves is treated in a standard approximate fashion through hydraulic jumps and bores (cf. Ref. 10).

The resulting 1D model equations comprise conservation of mass and momentum for water of depth $h=h(x,t)$ and velocity $u=u(x,t)$ in a contraction of width $b=b(x)$, where x is the streamwise horizontal direction and t is the time. That is, after averaging, we obtain

$$(hb)_t + (hbu)_x = 0, \tag{1a}$$

$$(hbu)_t + (hbu^2)_x + \tfrac{1}{2}gb(h^2)_x = -C_d^\star b|u|u, \tag{1b}$$

where subscripts with respect to t and x denote the respective partial derivatives, g is the acceleration due to gravity, and $C_d^\star$ is an experimentally determined drag coefficient. $C_d^\star$ is usually on the order of 10^{-3};[10] Pratt noted a measured value of $C_d^\star = 4.4\times 10^{-3}$.[13] We consider a uniform channel of width b_0 with a localized contraction where $b(x)<b_0$ is monotonically decreasing to a minimum nozzle width $b(x_c)=b_c$ from $x=0$ to $x=x_c$. In all experiments, this nozzle width occurs at the end of the channel and the contractions are linear.

We scale Eq. (1) as follows:

$$t=(u_l/b_0)t', \quad x=b_0x', \quad u=u_lu',$$
$$h=h_lh', \quad b=b_0b', \quad C_d=C_d^\star b_0/h_l, \tag{2}$$

using values u_l, b_0, h_l upstream of the contraction at $x=-x_l<0$ and an upstream Froude number $F_l=u_l/\sqrt{gh_l}$. The length x_c of the contraction then determines the (average) slope $\alpha=(b_0-b_c)/x_c$. The parameters appearing in the 1D dynamics are thus x_c, x_l, α, C_d, g, u_l, h_l, b_0, and b_c. The following dimensionless form of Eq. (1) emerges after dropping the primes:

$$u_t + uu_x + h_x/F_l^2 = -C_d u^2/h, \tag{3a}$$

$$(bh)_t + (buh)_x = 0. \tag{3b}$$

We define the nondimensional Froude number,

$$F = F_l u/\sqrt{h}. \tag{4}$$

Either $F_l=F_0$ for values u_0, b_0, and h_0 far upstream at a location $x=-x_l=-x_0$ near the sluice gate or $F_l=F_m$ for values u_m, b_0, and h_m at the entrance $x=-x_l=0$ of the contraction. After rescaling, the following parameters remain: F_l, $B_c=b_c/b_0$, as well as the scaled C_d, α, and dimensionless x_c and x_l.

First, consider steady-state solutions of Eq. (3). Hence, from Eqs. (3a) and (4), one finds

$$\frac{d[(1+F^2/2)h]}{dx} = -C_d F^2. \tag{5}$$

Since for steady flow $buh=Q$ from Eq. (3b) with the discharge Q as integration constant and $Q=1$ for our scaling, we derive

$$h = \left(\frac{QF_l}{Fb}\right)^{2/3} \quad \text{and} \quad \frac{dh}{dx} = -\frac{2}{3}\frac{h}{F}\frac{dF}{dx} - \frac{2}{3}\frac{h}{b}\frac{db}{dx}. \tag{6}$$

Combining Eqs. (5) and (6) gives

$$\frac{dF}{dx} = \frac{1}{2}\frac{(2+F^2)F}{F^2-1}\frac{d\ln b}{dx} - \frac{3}{2}\frac{C_d b^{2/3}}{(QF_l)^{2/3}}\frac{F^{11/3}}{F^2-1}. \tag{7}$$

At least for the separate cases (i) $C_d=0$ and $b=b(x)$ and (ii) $C_d>0$ and $b=b_0(=1)$, Eq. (7) can be solved analytically. We obtain for the inviscid case (i) $C_d=0$, $b=b(x)$ the solution

$$\frac{F_l}{F}\left(\frac{2+F^2}{2+F_l^2}\right)^{3/2} = b/b_0, \tag{8}$$

and for constant-width case (ii) $C_d>0$, $b=b_0$,

$$\frac{3}{2}\left(\frac{1}{F_l^{2/3}} - \frac{1}{F^{2/3}}\right) + \frac{3}{8}\left(\frac{1}{F^{8/3}} - \frac{1}{F_l^{8/3}}\right) = -\frac{3}{2}\frac{C_d b_0^{2/3}}{(QF_l)^{2/3}}(x+x_l), \tag{9}$$

where F_l is the Froude number and b_0 is the upstream width at $x=-x_l$. Either $x_l=x_0$ or $x_l=0$ and likewise for $F_l=F_0$ or $F_l=F_m$, where F_m is the Froude number at the contraction entrance. Smooth averaged 1D solutions exist as long as the flow is subcritical with $F<1$ or supercritical with $F>1$. In the inviscid case, the solution with $F=1$ at $x=x_c$ and $F_l=F_0$, for $x\le 0$ in Eq. (8),

$$F_0\left(\frac{3}{2+F_0^2}\right)^{3/2} = B_c, \tag{10}$$

demarcates the smooth sub- and supercritical flows in the F_0-B_c parameter plane, where $B_c=b_c/b_0$ is the scaled critical nozzle width; it is the thin solid line in Fig. 2. The Froude number is then constant in the channel upstream of the contraction whence $F_l=F_0=F_m$. For the well known critical condition $F=1$ at the nozzle, the flow is "sonic" or "critical" at the nozzle[9] such that the flow speed u equals the speed $\sqrt{h}/F_l$ of gravity waves (dimensionally u then equals $\sqrt{gh}$). This condition can be thought of as playing the role of a boundary condition in this system. It has been justified and analyzed by Vanden-Broeck and Keller[14] based on nonhydrostatic potential flow.

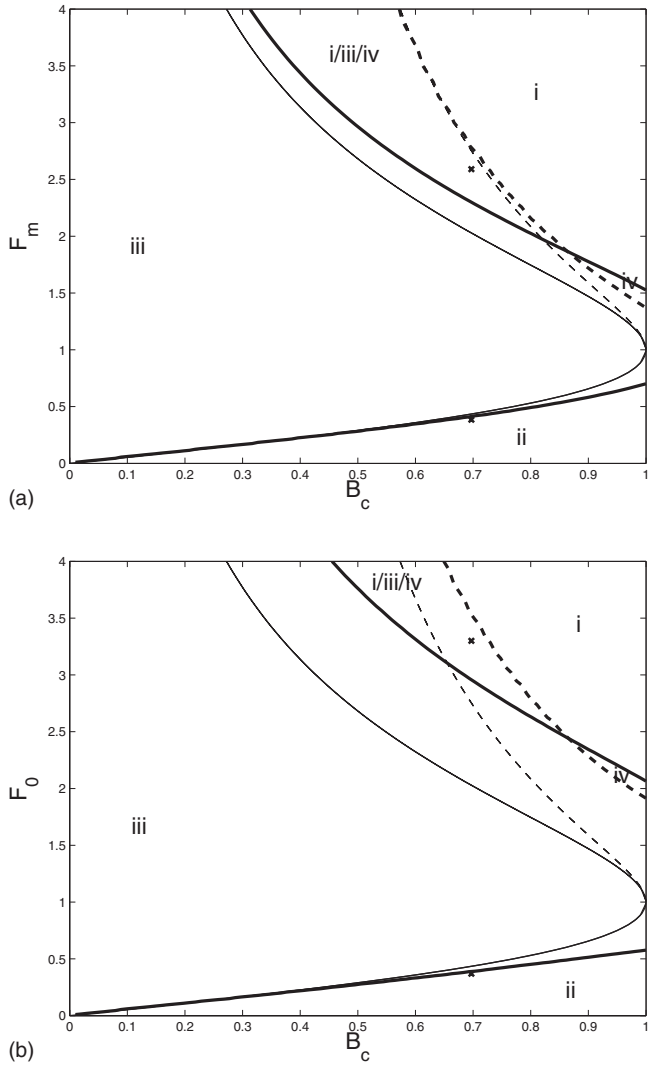

FIG. 2. (a) The F_m, B_c plane and (b) the F_0, B_c plane divided into regions of different (steady) flows: In region iii, upstream moving/steady shocks only; in region i/iii/iv, steady shocks in the contraction, upstream moving/steady shocks, and oblique waves or averaged smooth flows; in region ii, subcritical smooth flows are distinguished from flows in region iii by the absence of an upstream moving shock in the transient stage, and in region i, analysis predicts supercritical smooth flows, as the cross-sectional averages of the experimentally observed oblique waves. The solid lines demarcate the existence region of sub- and supercritical flows for inviscid and frictional flows (thin and thick lines). The dashed lines demarcate the extent of moving/steady upstream shocks also for inviscid and frictional flows (thin and thick dashed lines). The thick solid and dashed lines are for (a) $C_d^*=0.0037$, $h_0=0.0143$ m, $x_l=1.06$ m, and $L=0.465$ m and (b) $C_d^*=0.0037$, $h_0=0.0169$ m, $x_l=1.06$ m, and $L=0.465$ m.

Our approach is as follows when friction is nonzero $C_d>0$ for a localized (linear) contraction. Say, the Froude number F_l and depth h_l are known at a distance x_l+x_c upstream of the nozzle, where x_c is the length of the contraction along the channel. Either we take $F_l=F_0$ as the upstream Froude number or $F_l=F_m$ as the Froude number at the contraction with $x_l=0$. We integrate the ordinary differential equation [restating Eq. (7)],

$$\frac{dx}{dF} = \frac{2(F^2-1)}{(2+F^2)F\dfrac{d\ln b}{dx} - 3F^{11/3}C_d b^{2/3}/(QF_l)^{2/3}}, \tag{11}$$

with a fourth-order Runge–Kutta scheme, either starting from $x=-x_l$ given F_l or from $x=x_c$ at the contraction exit with $F=\lim_{\epsilon\downarrow 0} 1\pm\epsilon$ given B_c and then the slope α, the width $b=b(x)$, and the length x_c of the contraction. Note that given the fixed length of a contraction paddle L, we find $x_c = L\cos\theta_c$ with angle $\theta_c = a\sin[(b_0-b_c)/(2L)]$. For given sufficiently large $F_l>1$ or sufficiently small $F_l<1$ at $x=-x_l$, profiles of F, h, and u versus x can be calculated for sub- and supercritical flows by integrating from a point upstream of the contraction into the downstream direction. For flows with hydraulic jumps, the critical condition at the nozzle is $F=1$ and we calculate upstream starting at the nozzle and imposing the jump condition, where the downstream and upstream profiles match, see below. To obtain the critical curve between smooth super- and subcritical flows and flows with jumps, we start with $F=\lim_{\epsilon\downarrow 0} 1\pm\epsilon$, respectively, and integrate Eq. (11) upstream from the nozzle to $x=-x_l$ to find a new estimate F_l^*. However, we do not know the scaling F_l in Eq. (11) beforehand as it is part of the solution. The solution is therefore found iteratively. One can start with the inviscid $F_l=F_0$ as a function of B_c by using Eq. (10) and then proceeds with the newly obtained F_l^* until convergence is reached. While the boundary demarcation of smooth sub- and supercritical 1D solutions (10) is independent of the precise geometry of the contraction, this is no longer valid when friction is present.

For upstream moving shock solutions, we use a similar procedure, but instead of coupling the upstream conditions with the nozzle, we must couple the depth h_u and velocity u_u upstream of the shock to the values u_1 and h_1 just downstream of a shock moving at speed s (positive when moving upstream) and the depth h_c and velocity u_c at the nozzle. For a continuous width b, the weak formulation of Eq. (1) arises directly from the shock relations for Eq. (1) across the bore,[8,9]

$$(u_u+s)h_u = (u_1+s)h_1, \tag{12a}$$

$$(u_u+s)^2 = \frac{h_1}{2F_l^2}\left(1+\frac{h_1}{h_u}\right). \tag{12b}$$

In the inviscid case, we combine these with the Bernoulli and mass continuity equations in the contraction and the criticality condition (12e) to find

$$\tfrac{1}{2}u_1^2 + h_1/F_l^2 = \tfrac{1}{2}u_c^2 + h_c/F_l^2, \tag{12c}$$

$$u_1h_1b_1 = u_ch_cb_c, \tag{12d}$$

$$u_c^2 = h_c/F_l^2. \tag{12e}$$

If we scale by introducing $F_u=u_uF_l/\sqrt{h_u}$, $S=sF_l/\sqrt{h_u}$, $B_1=b_c/b_1$, and $H_1=h_1/h_u$, system (12) reduces after some manipulation to

$$\frac{1}{2}[F_u+(1-H_1)S]^2 = \frac{3}{2}H_1^2\left[\frac{F_u+(1-H_1)S}{B_1}\right]^{2/3} - H_1^3, \tag{13a}$$

$$(F_u+S)^2 = \tfrac{1}{2}H_1(1+H_1). \tag{13b}$$

When $H_1=1$, the limit when the jump in the depth is zero, Eq. (13) reduces to Eq. (10) for $F_u\leq 1$ and $B_1=B_c$. In the other limit, the shock has zero speed $S=0$ and arrests at the start of the contraction: It is the dashed thin line with $F_u>0$ and $B_1=B_c$ in Fig. 2. The thin solid line for $F_0<1$ and upper thin dashed line for $F_0>1$ demarcate a region in the F_0, B_c plane where moving shock and smooth solutions coexist, i.e., region i/iii/iv, while in region iii only upstream moving shocks exist.

In the frictional case, the shocks eventually become steady. We therefore take shock speed $s=0$. The Bernoulli relations valid in the inviscid case have to be replaced by Eq. (11) from the shock position to the nozzle. We calculate the shock arrested at the entrance of the contraction, analogous to the inviscid case. The expression (11) is integrated upstream from the nozzle with $F=\lim_{\epsilon\downarrow 0} 1-\epsilon$ to the entrance point of the contraction $x=0$ where a hydraulic jump occurs. The flow in between is subcritical. Denote the Froude number just downstream of $x=0$ as $F=F_1$ and upstream as F_m. Given the shock relations (12a) and (12b) with $h_u=h_m$, $u_u=u_m$, $F_u=F_m$, we deduce that $h_1/h_m=[-1+\sqrt{(1+8F_m^2)}]/2$. Note that in our scaling, $Q=1=h_1u_1=h_uu_u$. Hence,

$$F_m = \sqrt{8}F_1\Big/\left[-1+\sqrt{(1+8F_1^2)}\right]^{3/2} > 1. \tag{14}$$

We then integrate Eq. (11) further upstream from $F=F_m>1$ at $x=0$ to find our next estimate of F_l^* at $x=-x_l$. Generally, $F_l^*\neq F_l$, where F_l is the scaling used in Eq. (11). Hence, continue until convergence is reached and commence with the following inviscid result, $F_l=F_0(B_c)$, as a function of B_c. In the inviscid case, use of Eq. (8) with $F_l=F_1$ at the entrance of the contraction and $F_m=F_0>1$ to find $F_1=\sqrt{8}F_0/[-1+\sqrt{(1+8F_0^2)}]^{3/2}$ from Eq. (14) immediately gives

$$F_1\left(\frac{3}{2+F_1^2}\right)^{3/2} = B_c. \tag{15}$$

It is the dashed thin line in Fig. 2.

For fixed C_d, the parameter plane is formed by the existence or coexistence regions of four flow states: (i) Supercritical smooth flows, (ii) subcritical smooth flows, (iii) steady shocks or ones moving upstream in the inviscid limit, and (iv) steady shocks in the contraction. The inviscid and frictional flows are summarized in the parameter space F_m, B_c, C_d or F_0, B_c, C_d. The former holds for the scaling with values such as $F_l=F_m$ at the entrance of the contraction and the latter for a scaling with values $F_l=F_0$ further upstream (near the sluice gate). Note that the scaled C_d's have a different interpretation: In the former scaling, $C_d=C_d^\star b_0/h_m$ is used and in the latter one, $C_d=C_d^\star b_0/h_0$. We present both parameter planes F_m, B_c and F_0, B_c for the same dimensional value of $C_d^\star$ but adjusted dimensionless C_d with the choice $h_m=1.185h_0$ in Fig. 2; this choice corresponds to the case with $F_0=3.3$. The advantage of using F_m is that it excludes

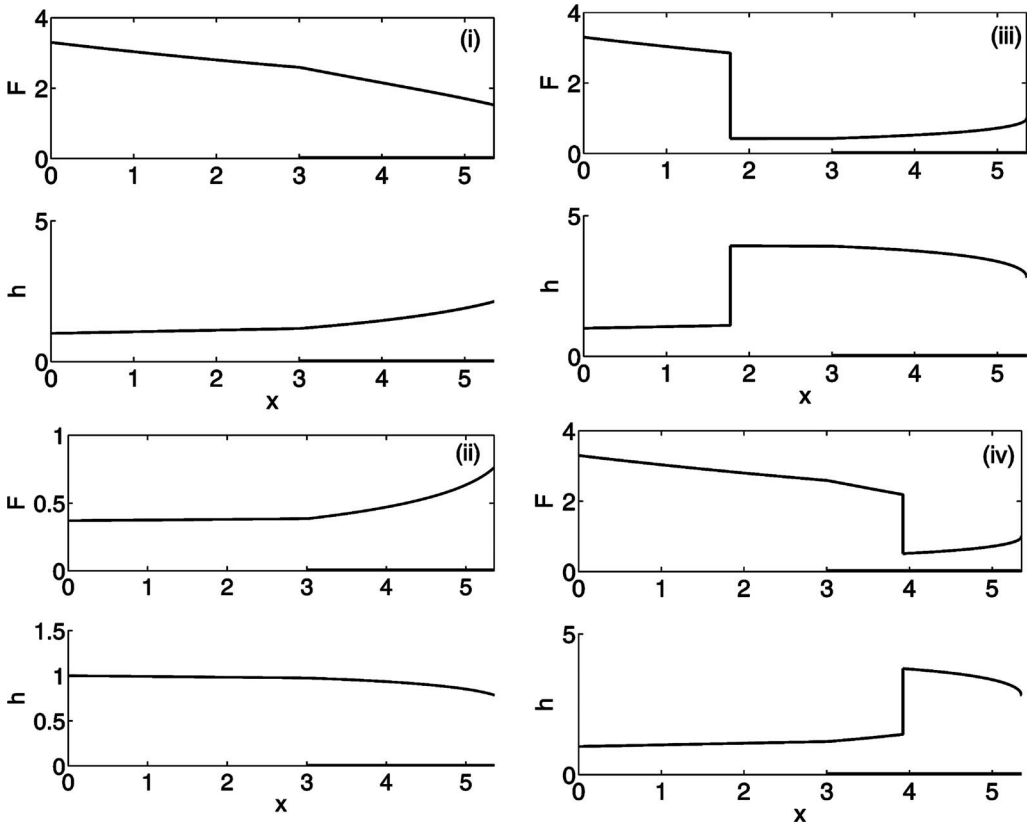

FIG. 3. Profiles of Froude number $F=F(x)$ and depth $h=h(x)$ as a function of downstream coordinate x for the four flow states: (i) supercritical flows with $F>1$, (ii) subcritical flows with $F<1$, (iii) upstream (steady) shocks, and (iv) reservoir with shock in the contraction. These profiles correspond with the crosses in Fig. 2. The extent of the contraction is indicated by a thick line on the x-axis.

shifts due to frictional effects in the uniform channel, while using F_0 matches better the experiments with F_0 measured at a fixed upstream point and nearly constant h_0. In Fig. 2 for $F>1$, solid thick and thin lines demarcate region iii with steady shocks, and upstream moving shocks for the inviscid case. Solid and dashed thin and thick lines demarcate region i/iii/iv with upstream moving/steady shocks and supercritical flows as well as a third reservoir shock state in the contraction, also for the inviscid case. Subcritical flows exist in a region, ii, below the thin and thick solid line for $F_m<1$ or $F_0<1$. Supercritical flows exist in region i. Finally, friction leads to a new region, iv, with the third reservoir shock state in the contraction and neither supercritical flows nor upstream moving/steady shocks. Flow profiles of the four flow states are displayed in Fig. 3. They correspond with the points marked by crosses in the parameter planes of Fig. 2.

A. Steady shock state in contraction

Baines and Whitehead's work[5] motivated us to search for an averaged steady reservoir state with a shock in the contraction. Consider the case with $C_d=0$. The depth h_1 and velocity u_1 at the upstream limit of a shock within the contraction are not the same as upstream depth h_0 and velocity u_0, and must be coupled to the values u_2 and h_2 at the downstream limit of the shock, which, in turn, are connected to the conditions u_c and h_c at the nozzle exit. For steady shocks, the shock speed is zero. Instead, the location x_s of the steady shock or the width of the channel $b_s=b(x_s)$ has become a new unknown. The seven equations for u_1, h_1, b_s, u_2, h_2, u_c, and h_c consist of mass conservation, Bernoulli conditions, the shock relation, and the critical condition:

$$u_0h_0b_0 = u_1h_1b_s = u_2h_2b_s = u_ch_cb_c, \tag{16a}$$

$$\tfrac{1}{2}u_0^2 + h_0/F_0^2 = \tfrac{1}{2}u_1^2 + h_1/F_0^2, \tag{16b}$$

$$\tfrac{1}{2}u_2^2 + h_2/F_0^2 = \tfrac{1}{2}u_c^2 + h_c/F_0^2, \tag{16c}$$

$$u_1^2 = \frac{h_2}{2F_0^2}\left(1 + \frac{h_2}{h_1}\right), \tag{16d}$$

$$u_c^2 = h_c/F_0^2. \tag{16e}$$

We solve this system and check the limits where the shock vanishes such that $h_1=h_2$ and where the shock is at the mouth of the contraction such that $b_s=b_0$ and $h_1=h_0$. Steady shocks are then found to exist in region i/iii/iv of the F_m, B_c and F_0, B_c planes demarcated by the thin solid and dashed lines in Fig. 2. In region i/iii/iv, moving shocks and smooth flows coexist.

Next, we investigate the stability of the (inviscid) solution to Eq. (16) with the method used in Baines and Whitehead.[5] They considered a particular perturbation of the depths and velocities. Again, we label the upstream and downstream limit of the velocity and depth at the shock as u_1, h_1 and u_2, h_2. The system is then linearized and solved for

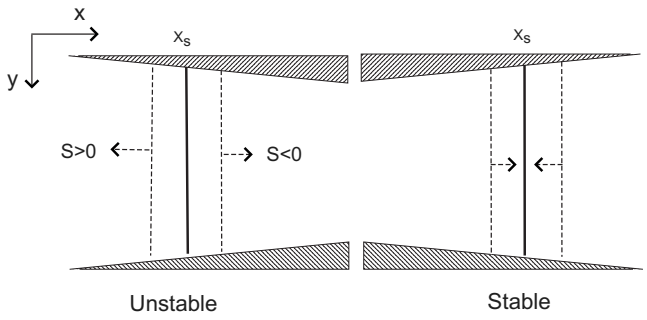

FIG. 4. Top view of the contraction. The speed of a bore will depend on the geometry of the channel at the unperturbed jump. A steady jump is unstable when for upstream displacements the resulting jump has an upstream velocity and, similarly, for downstream displacements the resulting jump has a downstream velocity.

the dependence of shock speed s (positive when moving upstream) on the displaced shock position b_s+b^ϵ with perturbations denoted by superscript ϵ. If the signs of b^ϵ and s are the same in a contracting channel, then the shock moves away from its previous location and is linearly unstable (see Fig. 4) and vice versa. First, the perturbed flow balances mass and momentum over the shock,

$$(u_1+u_1^\epsilon+s)(h_1+h_1^\epsilon)=(u_2+u_2^\epsilon+s)(h_2+h_2^\epsilon), \tag{17a}$$

$$(u_1+u_1^\epsilon+s)^2(h_1+h_1^\epsilon)+\frac{(h_1+h_1^\epsilon)^2}{2F_0^2} = (u_2+u_2^\epsilon+s)^2(h_2+h_2^\epsilon)+\frac{(h_2+h_2^\epsilon)^2}{2F_0^2}. \tag{17b}$$

Second, steady mass conservation holds upstream of the jump and thus

$$(u_1+u_1^\epsilon)(b+b^\epsilon)(h_1+h_1^\epsilon)=Q. \tag{18}$$

Third, the perturbation does not affect the far field momentum upstream E_1 or downstream E_2, so the Bernoulli constants are unchanged,

$$\frac{1}{2}(u_1+u_1^\epsilon)^2+\frac{(h_1+h_1^\epsilon)}{F_0^2}=E_1=\frac{1}{2}u_1^2+\frac{h_1}{F_0^2}, \tag{19a}$$

$$\frac{1}{2}(u_2+u_2^\epsilon)^2+\frac{(h_2+h_2^\epsilon)}{F_0^2}=E_2=\frac{1}{2}u_2^2+\frac{h_2}{F_0^2}. \tag{19b}$$

We are considering only small perturbation terms, so terms with superscript ϵ and s are of $O(\epsilon)$. Linearizing Eqs. (17)–(19) gives a system of six unknowns and five equations,

$$u_1^\epsilon h_1 b+u_1 h_1 b^\epsilon+u_1 b h_1^\epsilon=0, \tag{20a}$$

$$u_1^\epsilon h_1+s h_1+u_1 h_1^\epsilon=u_2^\epsilon h_2+s h_2+u_2 h_2^\epsilon, \tag{20b}$$

$$u_1 u_1^\epsilon+h_1^\epsilon/F_0^2=0, \tag{20c}$$

$$u_2 u_2^\epsilon+h_2^\epsilon/F_0^2=0, \tag{20d}$$

$$2h_1u_1(u_1^\epsilon+s)+h_1^\epsilon u_1^2+h_1h_1^\epsilon/F_0^2 = 2h_2u_2(u_2^\epsilon+s)+h_2^\epsilon u_2^2+h_2h_2^\epsilon/F_0^2. \tag{20e}$$

After some algebra, we obtain the relationship

$$S=\frac{F_1(1-u_1/u_2)}{(1-h_2/h_1)}B^\epsilon, \tag{21}$$

where $S=sF_0/\sqrt{h_1}$, $F_1=u_1F_0/\sqrt{h_1}$, and $B^\epsilon=b^\epsilon/b$. For any shock, the depth must increase going downstream, i.e., $h_1<h_2$, conservation of mass then gives $u_1>u_2$, thus Eq. (21) yields that the sign of S equals that of B^ϵ. In conclusion, steady shocks in the contraction region are unstable. An extended stability calculation with the same outcome is found in Appendix B.

III. EXPERIMENTS

Equations (1a) and (1b) are derived by assuming the fluid velocity and depth to be functions only of the distance x down the channel and time t. Dependence on the cross-channel coordinate y has thus been averaged out. This is a large simplification since the contraction geometry enforces the depth-averaged velocity to be 2D. In addition, the velocity profile will vary in depth. When the velocity normal to the channel walls is small relative to the downstream one, then we expect the 1D model presented to be asymptotically valid.

To assess the results of the 1D model, especially the presence of a stable reservoir state, a series of experiments was conducted in a horizontal flume. The flume was $b_0=0.198$ m wide and about 1.10 m long. Water entered one side of the flume via an adjustable sluice gate and dropped freely in a container at the other end. Linear contractions were made by two Plexiglas paddles held in place by tape. The water near the upstream sluice gate of the channel had a characteristic depth varying around $h_0=0.013-0.016$ m. The pumps used to recirculate the water after it left the downstream end of the flume could pump up to 0.005 m^3/s, but most experiments were conducted with discharges closer to 0.0003 m^3/s (giving $u_0=0.1-1.6$ m/s). Foam pads at the upstream side of the sluice gate were used to reduce turbulence generated by the pumps. For each experiment, Plexiglas paddles of length 0.3065, 0.32, or 0.465 m were inserted at the downstream end of the flume to form a linear contraction. Water discharge $Q=h_0u_0b_0$ and water depth h_0 near the sluice gate were varied via valves and adjustment of the gate height.

In model (1), we have neglected the effect of surface tension and viscosity and parametrized turbulent friction. These seem reasonable assumptions given the estimated Reynolds numbers, $\mathrm{Re}=u_0h_0/\nu=F_0\sqrt{gh_0}h_0/\nu$, with viscosity $\nu=10^{-6}$ m^2/s, between 1000 and 25 000 and Weber numbers, $\mathrm{We}=(\rho u_0^2h_0)/\sigma=\rho gF_0^2h_0^2/\sigma$, with gravitational acceleration $g=9.81$ m/s^2 and surface tension $\sigma=735$ dyn/cm $=0.0735$ N/m, between 1.8 and 560.

By adjusting the angle θ_c of the paddles forming the linear contraction at the downstream end of the flume and restricting the flow rate at the upstream end, we could vary F_0 between 0.2 and 4 and B_c between 0.6 and 1.

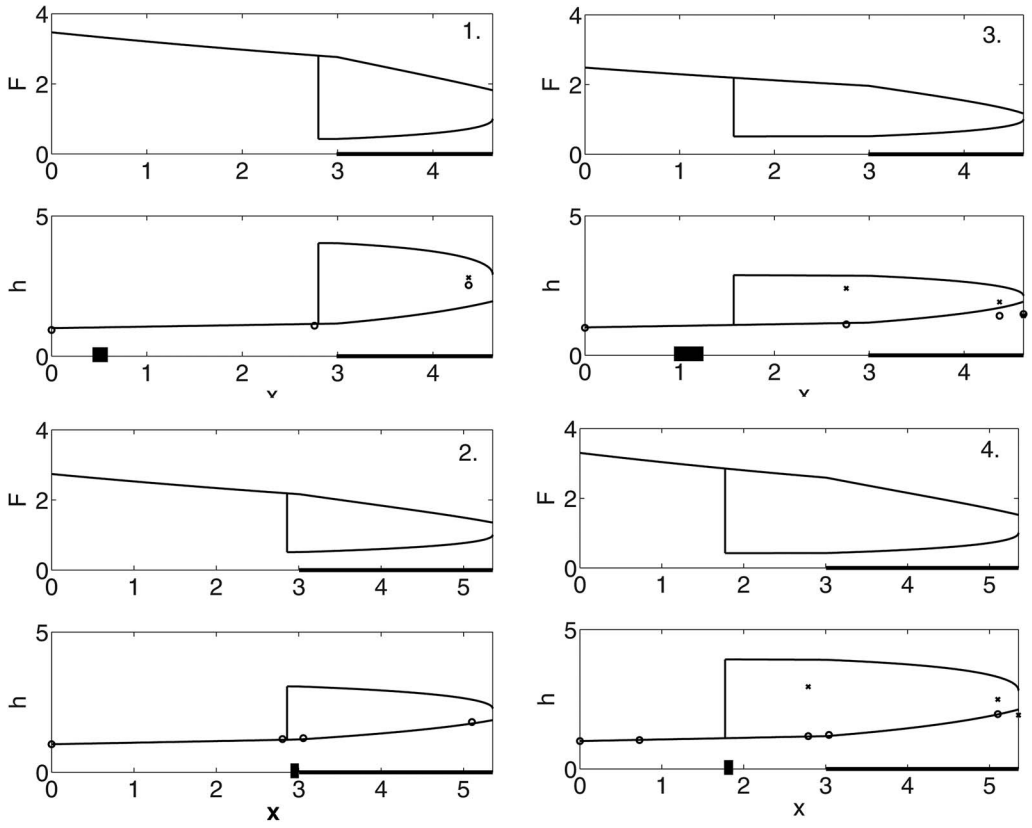

FIG. 5. Profiles and measurements of Froude number $F=F(x)$ and depth $h=h(x)$ as a function of downstream coordinate x in regime i/iii/iv for several flow states and paddle configurations: (1) $L_t=x_c+x_0=0.916$ m, $L=0.324$ m, $h_0=0.015$ m, $F_0=3.47$, $B_c=0.697$, $C_d^\star=0.0037$; (2) $L_t=1.06$ m, $L=0.465$ m, $h_0=0.016$ m, $F_0=2.74$, $B_c=0.798$, $C_d^\star=0.0037$; (3) $L_t=0.916$ m, $L=0.324$ m, $h_0=0.016$ m, $F_0=2.487$, $B_c=0.798$, $C_d^\star=0.0037$; (4) $L_t=1.06$ m, $L=0.465$ m, $h_0=0.014$ m, $F_0=3.3$, $B_c=0.697$, $C_d^\star=0.0037$. These profiles correspond to data in Fig. 6. The extent of the contraction is indicated by the thick line and the location of the upstream shock by a very thick line on the x-axis. The values of h_0 and F_0 have been adjusted within their ranges of uncertainty to make the best fit of the calculated and measured shock positions. Measurements of the oblique waves (circles) and the shock state (crosses) have been made in unison. Hence, we show both solution branches in one graph.

In the experiments, we observed upstream moving shocks—as expected. In the supercritical flow regime where the 1D model predicts smooth flows, we see oblique waves with a smooth cross-sectional average. Although the 1D model considered so far is indeed a smooth cross-sectional average of a 2D flow, it still has some predictive value. At the transition between moving and oblique waves, also, steady upstream shocks emerged and steadied due to turbulent drag. Smooth subcritical flows were also observed. The one-dimensional analysis yields an averaged solution in the contraction. Beyond the contraction, the flow accelerates in a free jet and Eq. (8) suggests that there may be a smaller nozzle width in the jet where the flow becomes critical. Consequently, this subcritical flow does not need to be critical at the minimum contraction width.

A comparison between measurements and 1D calculations is made in Fig. 5. Four different configurations have been considered in some detail within region i/iii/iv with multiple steady states. Whereas the comparison between theory and measurements for state iii with oblique waves is good, the agreement between the calculated upstream shocks and the measurements is less good. We used a best fit with one value $C_d^\star=0.0037$ and adjusted h_0 and F_0 for each configuration in a best fit to the observed and measured shock position. The latter fails only for the case in Fig. 5(1). Reasons for the imperfect match are hypothesized to be the difficulty in the determination of $C_d^\star$ in combination with the simplicity of the quadratic friction law as model for the turbulence, and the 2D nature of the flow in relation to the form of the critical condition at the nozzle. Following classical approaches for flow in a channel, the friction factor becomes weakly dependent on the Reynolds number as $C_d^\star \approx (3/64)0.316\mathrm{Re}^{-0.25}$ for smooth channel walls.[15] Hence, $C_d^\star \approx 0.0012$ in the four cases of Fig. 5 and the variations caused by depth changes are only about 30%. Roughness effects of the channel bottom and side walls likely attribute to larger values of $C_d^\star$ such as the value $C_d^\star=0.0037$ we have adopted. An overview of the observed flows is given in the parameter planes in Fig. 6. The agreement between the experimental data and the 1D calculations is fairly good even though the adopted single value of $C_d^\star=0.0037$ and single value of h_0 has its shortcomings. Furthermore, in the calculation for Fig. 6, we use one configuration for certain L and $L_t=x_c+x_0$, while the data concern four configurations with some variations in L and L_t. To wit, by inspection of Fig. 6, the squares for upstream shocks fall nearly all in region iii, the circles for oblique waves in region i, the plus signs for subcritical flows in region ii, and the diamonds, circles, and stars in region i/iii/iv.

However, the main purpose of the experiments was to

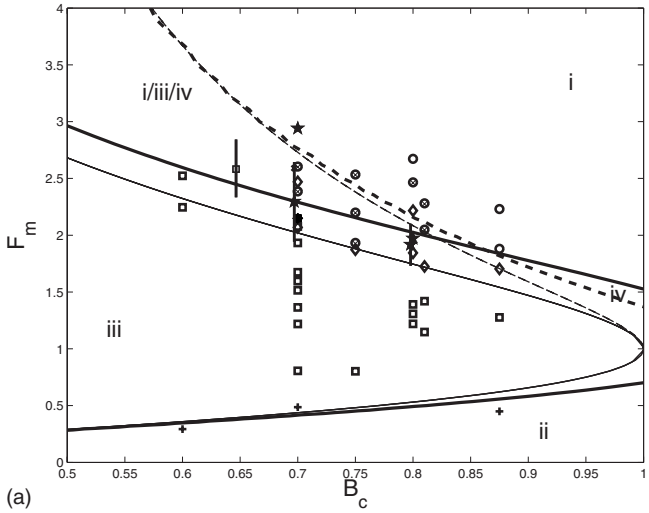

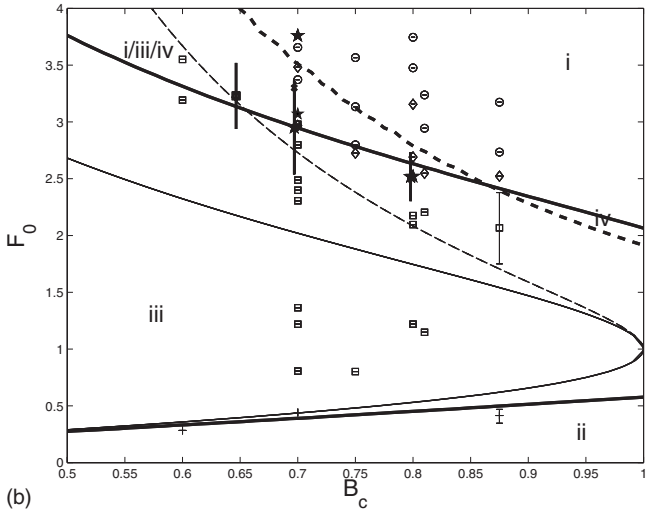

FIG. 6. The different regions, i–iv, in the (a) F_m, B_c and (b) F_0, B_c parameter planes superimposed on the observations using unscaled (a) $C_d^\star=0.0037$, $h_m=0.017$ m and (b) $C_d^\star=0.0037$, $h_0=0.014$ m. In (a), the observations with Froude numbers $F_0<0.5$ and $F_0>1.4$ have been adjusted to the respective Froude numbers F_m at the contraction entrance by using the measured F_0 and h_0 at the upstream location where the depth was measured. Observed flows: Plus signs are smooth flows, squares are upstream moving shocks, diamonds are steady shocks, and circles are oblique waves. The solid stars concern the flows as in Fig. 8 with three possible states for different configurations and paddle lengths. Some indicative error bars have been displayed.

investigate the existence and stability of steady shocks in the contraction region. If we solve system (13) for the shock speed, we see that increasing the upstream flow rate decreases the speed of a shock. This was observed experimentally. It allowed us to adjust the flow rate to arrest a moving shock by increasing the upstream flow rate. With this procedure, it was easy to find steady shocks at any point upstream of the contraction. In the contraction, the flow is sensitive to small adjustments in flow rate, yet by inserting a paddle into the flow and pushing the shock in the appropriate direction, we were able to balance shocks in the contraction region. These shocks differ from the steady ones observed upstream of the contraction, in that they have a distinct 2D horizontal structure (see Fig. 7) and oscillate somewhat in both shape

FIG. 7. (Color) The structure of the 2D hydraulic jump in the contraction is akin to a Mach stem in a nozzle in gas dynamics. (Top view) Oblique waves originate at the beginning of the contraction and are joined by a "stem" roughly perpendicular to the channel walls. Here, $F_0=3.07$, $B_c=0.7$ corresponding to a star in Fig. 6.

and position. They are analogous to Mach stems in gas dynamics.[8]

In the flow regime where these Mach-stem-like shocks in the contraction region exist (region i/iii/iv in Fig. 6), we also observed steady shocks just upstream of the contraction entrance and oblique waves in the contraction. For certain fixed flow rates, the three flow states coexist. This regime with three stable states was observed experimentally for several geometries and flow rates, indicated by five stars in Fig. 6. We confirmed the existence of the middle reservoir state for three sizes of paddles, and for the longest pair of paddles, this state persevered in a one-paddle setup with the same $B_c=0.798$. It seems to only occupy part of region i/iii/iv as the two stable flow states with upstream shocks and oblique waves persist for more parameter values. The setup and measurements used were not accurate enough to determine the existence region beyond measurement errors. Nevertheless, the reservoir state would persist for a small range of flow rates adjusted by opening and closing valves and accompanying shifts of the Mach stem; also, hysteresis was observed. We could perturb the flow from one state to another. A first temporary restriction of the flow allowed us to perturb from oblique waves to the Mach-stem-like shock and via a second restriction to an upstream steady shock. Vice versa, by temporarily and locally accelerating the flow, it perturbed an upstream shock into steady flow with a hydraulic jump in the contraction, and then again to steady flow with oblique waves. The acceleration or restriction mentioned here was imposed simply by either manually placing a large Plexiglas paddle in the flow or pushing water in the appropriate direction (see the results in Fig. 8).

A. Discussion

The observations are superimposed in Fig. 6 over the regions of different flow types as predicted by the 1D hydraulic model using turbulent friction $C_d^\star=0.0037$. There are three phenomena of significant interest observed experimentally that were not predicted well by the 1D model. First, instead of 1D smooth supercritical flows, oblique waves exist. These are quintessential 2D phenomena and cannot be captured by the 1D model. Yet, they can be considered as the

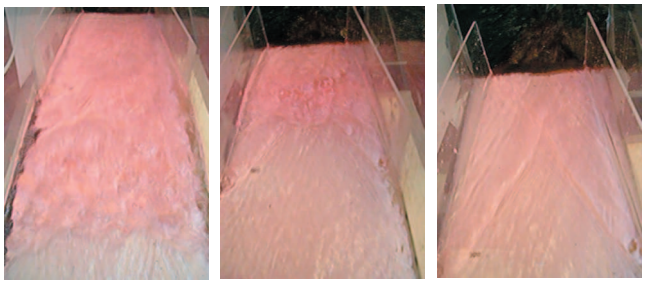

FIG. 8. (Color) Multiple states appear for $F_0=3.07$ and $B_c=0.7$ marked by a star in Figure 6. From left to right, these states are an upstream steady shock, the reservoir state, and oblique waves. Each transition is induced by blocking or pushing the flow with a small paddle (enhanced online).

smooth 1D average of the 2D supercritical flow. Even though the governing equations for the cross sectionally averaged height and velocity are different from the 2D ones, the 1D analysis matched the data well.

Second, there is a notable shift in the boundaries of the different flow types by the inclusion of turbulent friction, especially in Fig. 6(b). Due to the effect of friction, also steady upstream shocks were observed in multiple experiments. The matching of the 1D model with the experimental data appears best for $C_d^\star=0.0037$ and $h_0=0.014$ m and $h_m=0.017$ m in the F_m,B_c- and F_0,B_c-parameter planes (see Fig. 6). Presentation of the results in these parameter planes is problematic as the friction parameter C_d generally varies per measurement as h_0 and h_m vary. The latter is clear from Table I, where we have tabulated the measurements and calculated several parameters.

Finally, the most notable difference between the predicted flow types and the observed flow types concerns the existence and nature of the stable reservoir state with a Mach stem. While the 1D analysis for $C_d=0$ predicts the existence of an averaged unstable shock, it does neither explain its complex 2D nor its small region of stability within the larger region where states i and iii coexist. We therefore conclude that the 1D frictional analysis leads only to an approximate correspondence with the observations. Improvements are required by including a better frictional model and two-dimensional effects.

IV. 2D EFFECTS

The supercritical flows observed consisted of steady oblique hydraulic jumps angled to the channel walls, as we saw in the rightmost image of Fig. 8. These oblique waves are not captured by the 1D hydraulic theory presented. We will therefore first give a theoretical analysis of 2D supercritical flows and compare these with the 1D hydraulic predictions and numerical flow simulations. All these flows are taken inviscid except for local energy dissipation in bores and hydraulic jumps. Subsequently, predictions of oblique jumps starting from the onset of the contraction are compared to measurements.

A. Existence of 2D oblique hydraulic jumps

Our aim is to determine for which values of upstream Froude number F_0 a regular pattern of oblique and intersecting hydraulic jumps exist in a channel with linearly contracting walls and a nozzle of width B_c.

The inviscid flow upstream of the contraction is uniform with constant Froude number F_0, depth h_0, and speed $\mathbf{v}=U_0(1,0)$. Collision of this uniform channel flow with the contraction walls leads to two oblique hydraulic jumps. For low enough Froude number, these oblique jumps meet symmetrically at the center of the channel to generate two new oblique jumps, which can reflect again against the contraction walls, and so forth. A pattern of triangles and quadrilaterals results beyond the first oblique jumps in which the flow is alternately parallel to a contraction wall or parallel to the channel centerline. In each polygon, the flow is uniform with a constant Froude number, decreasing in value to the next polygon downstream. The angles of the oblique jumps with the contraction walls relative to the channel walls are numbered oddly, θ_{2m+1}, and the angles of the oblique jumps at the centerline evenly, θ_{2m+2}, with integer $m\geqslant 0$ (see the sketch in Fig. 9). The angle of the contraction is denoted by θ_c.

Consider a parallel shallow water channel flow with constant depth h_{2m}, velocity $\mathbf{v}=U_{2m}(1,0)$, and Froude number F_{2m}, colliding with two oblique walls under angles $\pm\theta_c$ (see Fig. 9). For supercritical flow, water piles up against the walls in a symmetric fashion relative to the channel centerline behind two oblique hydraulic jumps. The oblique hydraulic jump has an angle θ_{2m+1} relative to the parallel flow; downstream of this jump, depth h_{2m+1}, velocity $\mathbf{v}_{2m+1}=U_{2m+1}(\cos\theta_c,-\sin\theta_c)$, and Froude number F_{2m+1} are con-

TABLE I. Summary of several observations, especially in the regime with three stable flow states. The measurements in Fig. 5 constitute cases (1)–(4).

Q (0.001 m^3)	h_0 (0.01 m)	L_t (m)	L (m)	B_c	F_0	Case	Year
0.26–3.39	1.3	1.10	0.3065	0.6–0.88	0.28–3.65	38×	2005
4.0	1.4	0.92	0.324	0.7	3.86	(1)	2007
3.2	1.6	0.92	0.324	0.8	2.55	(3)	2007
3.1	1.4	1.06	0.465	0.7	2.95	(4)	2007
3.0	1.6	1.06	0.465	0.8	2.46	(2)	2007

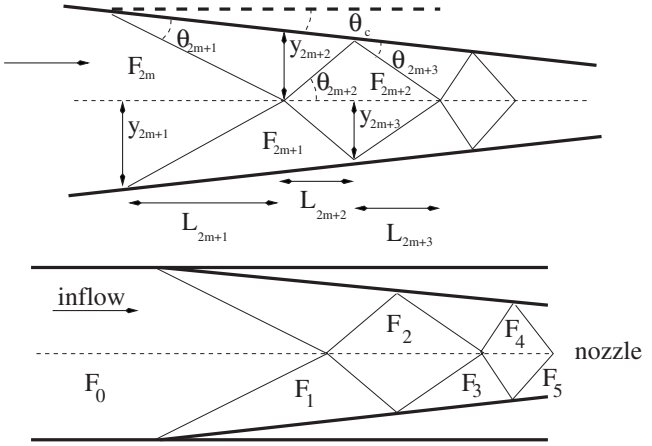

FIG. 9. Sketch of the oblique hydraulic jumps (thin solid lines) within the contraction and the definition of some of the variables involved. The centerline of the channel is dashed. Channel walls are thick lines.

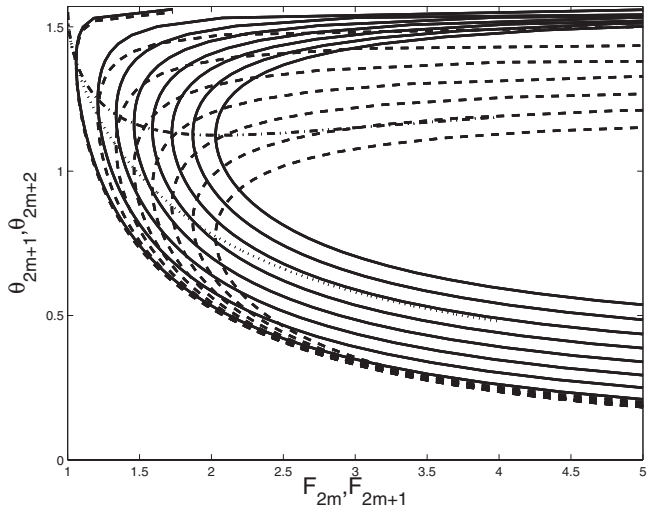

FIG. 10. Given various fixed angles $\theta_c=0.01, 0.0486, \ldots, 0.35$ (going from left to right) of the contraction walls, the odd θ_{2m+1} and even θ_{2m+2} angles of the associated oblique jumps have been calculated as a function of Froude numbers F_{2m} (solid lines) and F_{2m+1} (dashed lines), respectively.

stant. Classical 2D theory for oblique hydraulic jumps or shocks immediately yields the desired relations for the odd shocks,

$$\frac{h_{2m+1}}{h_{2m}} = -\frac{1}{2} + \frac{1}{2}\sqrt{1 + 8F_{2m}^2 \sin^2 \theta_{2m+1}} = \frac{\tan \theta_{2m+1}}{\tan(\theta_{2m+1} - \theta_c)}, \tag{22a}$$

$$\frac{U_{2m+1}}{U_{2m}} = \frac{\cos \theta_{2m+1}}{\cos(\theta_{2m+1} - \theta_c)}, \tag{22b}$$

$$F_{2m+1}^2 = F_{2m}^2 \frac{\cos^3 \theta_{2m+1} \sin(\theta_{2m+1} - \theta_c)}{\cos^3(\theta_{2m+1} - \theta_c)\sin \theta_{2m+1}} \tag{22c}$$

(cf. Refs. 7, 8, and 1). Likewise, for even shocks, one finds

$$\frac{h_{2m+2}}{h_{2m+1}} = -\frac{1}{2} + \frac{1}{2}\sqrt{1 + 8F_{2m+1}^2 \sin^2(\theta_{2m+2} + \theta_c)} = \frac{\tan(\theta_{2m+2} + \theta_c)}{\tan \theta_{2m+2}}, \tag{23a}$$

$$\frac{U_{2m+2}}{U_{2m+1}} = \frac{\cos(\theta_{2m+2} + \theta_c)}{\cos \theta_{2m+2}}, \tag{23b}$$

$$F_{2m+2}^2 = F_{2m+1}^2 \frac{\cos^3(\theta_{2m+2} + \theta_c)\sin \theta_{2m+2}}{\cos^3 \theta_{2m+2} \sin(\theta_{2m+2} + \theta_c)}. \tag{23c}$$

Note that Eq. (23) equals Eq. (22) by replacing $\theta_{2m+2}+\theta_c$ with θ_{2m+1} and subsequent shifting of other indices.

Given the contraction angle θ_c, there are relations between Froude numbers F_{2m} in Eq. (22a) and F_{2m+1} in Eq. (23a) and angles θ_{2m+1} and θ_{2m+2}, respectively. These have been displayed in Fig. 10 as solid and dashed lines, respectively, for various values of contraction angle θ_c. It is important to notice that below certain values of the Froude number, no oblique jump can exist; these minimum Froude numbers larger than unity have been indicated by the dashed-dotted and dotted lines, respectively.

While in 1D hydraulic theory the demarcation of the supercritical flow region was given by the criticality of the Froude number at the nozzle, the situation is more complex in the 2D setting.

- A pattern of oblique hydraulic jumps fails to exist within the contraction below a critical F_0 when no solutions exist for θ_{2m+1} in Eq. (22a) or θ_{2m+2} in Eq. (23a).
- It fails to exist when the Froude number of the last polygon entirely fitting within the contraction just falls below 1. Hence, only the Froude number of the last cutoff polygon of the pattern is allowed to be less than 1 for supercritical flow patterns to exist. The last polygon is cut off as no new polygon piece with the above oblique hydraulic jumps can enter the contraction anymore for a subcritical Froude number. The transition from supercritical to subcritical flow could then only occur across the last pair of oblique hydraulic jumps.

See Fig. 11 for a few oblique-wave profiles at this transition. As in the 1D setting, we heuristically assume that no flow information from beyond the nozzle can travel upstream. This is the case in our experiments where the flow after the nozzle becomes a free falling jet and in the probing 2D simulations below in which the channel widens again after the nozzle to freely exit thereafter. However, it is not the case when obstacles further downstream, or walls in a closed basin, block the downstream flow and (eventually) lead to information traveling upstream of the contraction nozzle.

For the minimum value of upstream Froude number $F_0 > 1$, it turns out that either a whole number of polygon patterns fits within the contraction or that the last polygon pattern only partly fits within the contraction with a small last and cutoff polygon where the Froude number is subcritical. A series of numerical simulations of the 2D shallow water equations revealed these conditions. In both cases, supercritical flow patterns exist for a minimum Froude number F_0,

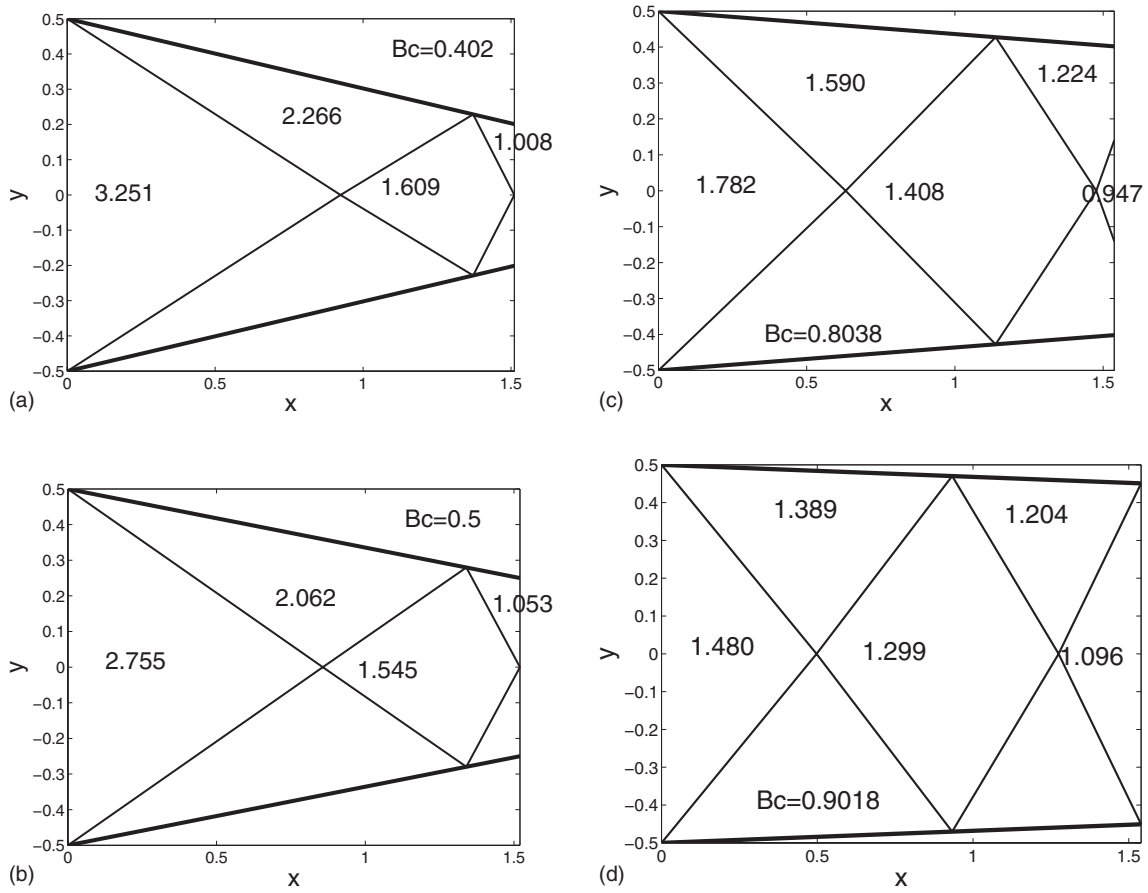

FIG. 11. Oblique jump patterns within the contraction for several values of B_c and minimal value of F_0, and $L=0.3065$ m in scaled coordinates. The thick outer lines denote the contraction walls; the thin lines denote the oblique jumps. Values of the Froude numbers have been displayed within each polygon.

which do not allow information to flow further upstream than the last set of oblique jumps either completely or partly filling the contraction near the nozzle. These 2D numerical simulations are based on space and space-time discontinuous Galerkin finite element methods, which are second order in space and time. The algorithms and codes used have been verified against rotating and nonrotating exact solutions and validated against experiments and bore-vortex interactions in Refs. 16–19. We predominantly used grids of 175×40 elements and ran a few cases with double resolution as a verification. Our scaled computational domain with $x\in[0,3.5]$ and $y\in[-0.5,0.5]$ consisted of a small inflow channel before the contraction, the contraction, and then a diverging channel with outflow boundary conditions based on the nonlinear characteristics.

In a semianalytical way, we obtained the minimum Froude number F_0 with supercritical flow patterns for given θ_c by using a fast shooting method in combination with the above-mentioned critical conditions and the following algorithm to calculate the jump angles. By using the information displayed in Fig. 10, we either know for which Froude numbers the angles cease to exist and must stop or we must stop when the calculated Froude number in the next downstream polygon falls below unity.

The algorithm to find the jump angles within the contraction starts with an upstream F_0 and the known half-channel width $y_1=b_0/2(=\frac{1}{2})$. Given $F_{2m+1}>1$ and half-width $y_{2m+1}>B_c/2$ midway, we find θ_{2m+1} from Eq. (22a). Geometric considerations, using Fig. 9, then yield the length of the polygon along the centerline to the intersection point of the pair of oblique jumps,

$$L_{2m+1}=y_{2m+1}/\tan\,\theta_{2m+1}, \tag{24}$$

while the next Froude number F_{2m+1} follows from Eq. (22c). The half-width at that intersection point is

$$y_{2m+2}=L_{2m+1}(\tan\,\theta_{2m+1}-\tan\,\theta_c). \tag{25}$$

Likewise, given $F_{2m+1}>1$ and half-width $y_{2m+2}>B_c/2$ midway, we find θ_{2m+2} from Eq. (23a). Furthermore,

$$L_{2m+2}=y_{2m+2}/(\tan\,\theta_{2m+2}+\tan\,\theta_c), \tag{26}$$

$$y_{2m+3}=L_{2m+2}\tan\,\theta_{2m+2}, \tag{27}$$

and F_{2m+2} follows from Eq. (23c).

The shooting method is as follows. We choose a value of B_c. The first or "left" guess is an upstream Froude number F_0 based on the 1D inviscid case. This value is too low: The resulting pattern will not reach the end of the contraction either because no new pair of oblique wave eventually exists or because the Froude number drops below 1. The next or "right" guess of F_0 is chosen such that the oblique-wave pattern extends beyond the nozzle, in which case we stop. Subsequently, we iterate based on linear estimates between left and right values of F_0 such that the pattern either does

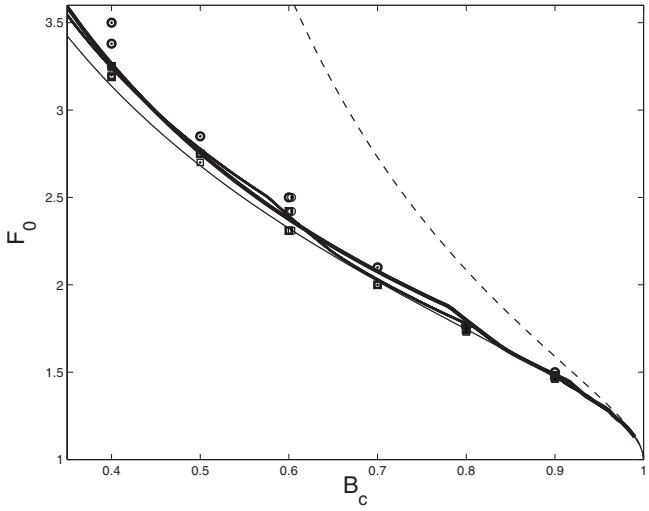

FIG. 12. The demarcation between supercritical (smooth) solutions and upstream moving jumps is determined with 1D hydraulic theory, 2D theory for oblique hydraulic jumps, and by numerical simulations. A comparison is made between 1D theory (thin line), 2D theory for paddle lengths $L=0.305$ m (thicker line) and $L=0.465$ m (thickest line), and numerical simulations for $L=0.305$ m (open circles and squares) and $L=0.465$ m (open circles and dotted squares). Simulations are largely done in a scaled domain $x\in[0,3.5]$ with 175×40 elements and thus scaled paddle lengths L/b_0 (for $b_0=0.198$ m). Indeed, the curves and symbols are close together, well within the error bars associated with the laboratory measurements.

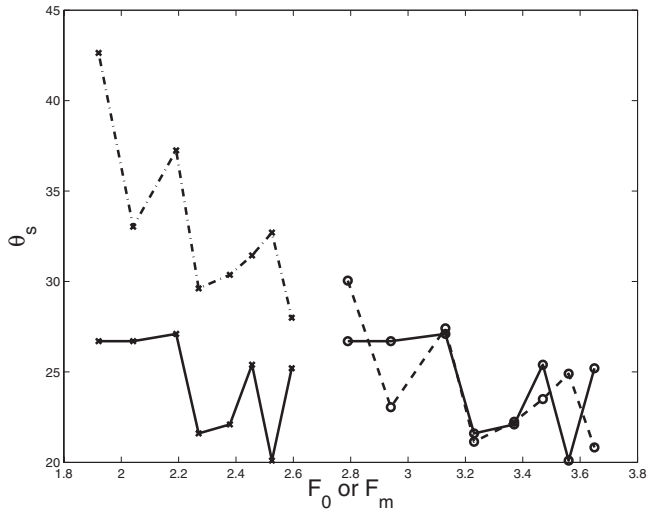

FIG. 13. The angle θ_s between the wall and the oblique wave is plotted against the Froude number F_0 at the sluice gate or a dissipation corrected Froude number F_m at the entrance of the contraction 0.8 m further downstream. Solid lines: Data, with circles for F_0 and with crosses for $F_m<F_0$. Dashed(-dotted) lines: Theoretical calculation of θ_s given F_0 (circles) or F_m (crosses) based on Eq. (22a).

not reach the nozzle or passes it. Due to the two stopping criteria for the existence of the oblique-wave pattern, the above iteration converges but often not to the minimal value of F_0 as it may fail to approach the minimal F_0 from below. We therefore start the iteration again with the inviscid 1D estimate of F_0 as the left value of F_0, as before, and as the right value, the outcome of the previous iteration minus a small number, $F_0-\epsilon$ with $0<\epsilon\ll1$. This iteration setup either converges to the value of $F_0-\epsilon$, essentially the value obtained in the first iteration, or a smaller value of F_0. The above analytical expressions are used and derivatives thereof in combination with numerical routines for finding the required angles for which various expressions become zero.

Results have been obtained for two of our fixed paddles with $L=0.3065$ and 0.465 m, implying that the contraction lengths change a bit for varying angles θ_c. For some contraction angles, we show the oblique hydraulic jump patterns for the minimum Froude number for which they exist (Fig. 11). These patterns show that while the contraction is long compared to the channel walls with a small aspect ratio, the oblique jumps have sharper angles with aspect ratios even bigger than unity. 2D effects therefore become more important in the determination of the supercritical flow region. Nevertheless, in Fig. 12, the demarcation (thick and thickest solid curves) based on these 2D calculations in the F_0,B_c-parameter plane lie very close to the thin demarcation curve given by the asymptotic 1D hydraulic theory [from Eq. (10)]. When the aspect ratio between the channel width and paddle length lies above unity, the departure between the 1D and 2D theory becomes of course (more) distinct, as expected. The numerical simulations indicated by circles for supercritical flows with oblique jumps and squares for upstream moving bores confirm these new calculations. The combination of two requirements, either the existence of the oblique angles or $F>1$ except beyond the last pair of oblique hydraulic jumps, introduce the wavy character in the demarcation curves as one requirement takes over from the other. The curves are slightly different due to the alteration in paddle length. The above existence criterion is somewhat heuristic and not mathematically rigorous but has been verified against numerical simulations and the notion that these supercritical patterns can only exist for certain Froude numbers. In addition, the above calculations hold for the linear contraction only, even though the generic outcome is expected to be robust, at least for nearly linear contraction channels.

B. Observed oblique jump angles

The angle θ_s between the wall and the oblique waves is plotted in Fig. 13 against the Froude number F_0 at the sluice gate or a dissipation corrected Froude number F_m at the entrance of the contraction at $x_0=0.8$ m downstream of this gate. The Froude number F_m is obtained analytically by using relation (9) for $C_d^\star=0.0037$. Both the experimental results of θ_s (solid lines) versus the upstream Froude number F_0 and a dissipation corrected Froude number F at the entrance of the contraction are given, as well as predictions (dashed and dashed-dotted lines) based on Eq. (22a) for $m=0$. While the inviscid predictions seem reasonable, the friction corrected results are not. Only for very small values of $C_d^\star=0.000\,12$ are the results reasonable (cf. numerical calculations by Ambati and Bokhove[17]). The latter value of friction seems too small. A careful examination of (all snapshots containing) these oblique waves show no sign of local wave breaking at the surface so characteristic in hydraulic jumps. Additional movies of the experiments often show capillary surface ripples, sometimes preceding the main oblique waves. It

seems to indicate that surface tension may play a secondary role in these small-amplitude waves. However, three-dimensional turbulent effects may also be important as deviations from the depth-averaged variables may cause changes. Further investigation is required to explain these oblique waves better, e.g., by adding some three-dimensional effects[20] and surface tension.

V. SUMMARIZING REMARKS

We presented an analytical and experimental study of hydraulic shallow water flow through a linearly contracting channel. Analytically, a new steady state was found in a 1D cross-sectional averaged model. As in Baines and Whitehead,[5] who found an unstable steady jump on the upstream side of an obstacle, the 1D steady jump in the contracting region was shown to be linearly unstable for flows inviscid except at hydraulic jumps.

An experimental apparatus consisting of a horizontal channel with a sluice gate at its beginning and a linear contraction at its end was constructed to investigate our new 1D hydraulic theory with bulk friction. Steady upstream jumps, supercritical weak oblique waves, and subcritical smooth flows were observed. Turbulent drag was a necessary addition to obtain fairly good agreement between observations and predictions of the 1D hydraulic model. In addition to oblique 2D waves, corresponding to the averaged supercritical state in the 1D analysis, we observed a steady 2D bore akin to a Mach stem in gas dynamics. The latter led to the formation of a reservoir in the contraction. This apparently novel state (see Fig. 7) was experimentally stable for certain F_0, b_c values and appeared to correspond to the averaged steady 1D hydraulic jump; this 1D jump was theoretically found to be unstable in the absence of bulk (turbulent) friction.

It seemed therefore less likely that the reservoir state would be observed in the parameter regime where three steady states could formally exist. This was indeed the case experimentally because steady flows with a Mach-stem reservoir in the contraction were never the preferred steady state emerging in the experiment. In order to observe such flows with a Mach stem, it was necessary to find the appropriate flow regime and then to force the flow artificially to hop to this metastable state. In practice, this was done by inserting a paddle in the flow and sweeping water downstream away from the upstream steady shock until it moved to the steady flow with a Mach stem. The 1D analysis predicts a region with three coexisting (stable) states but also a small region with only the reservoir state around $F \approx 1$, $B_c \approx 1$ (akin to a region in Ref. 21). In the experiments, the reservoir state oscillates slightly around a stable equilibrium and has a 2D horizontal structure; it also only occupies part of the region of the parameter plane where the other two states coexist. More research is required to explain and understand these experimental findings.

The idea of perturbing the flow around an unstable state motivated both our analysis and experiments. We were able to perturb a state with Mach stem to states with steady upstream jumps and oblique waves. We created these perturbations both artificially, with a Plexiglas paddle, and more geophysically by an avalanche of buoyant beads. In Fig. 14, we used an upstream avalanche of polystyrene beads and the resulting deceleration of the flow was sufficient to perturb the flow from a state with oblique waves to one with upstream steady shocks. It is a finite amplitude perturbation. The analysis and experiments shown here and in Ref. 1 form a basis for further experimental and theoretical work on the hydraulics of multiphase flows for slurries with water and floating particles. The multiphase system proposed by Pitman and Le[22] may be a good candidate to study the 1D and 2D hydraulics of such slurries.

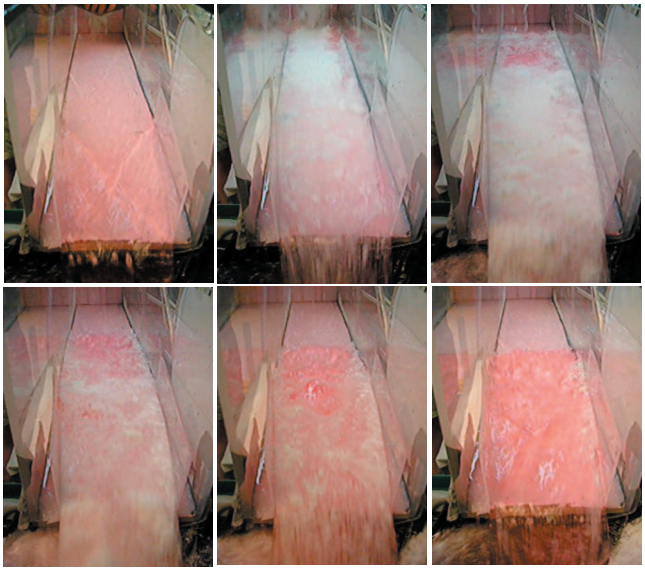

FIG. 14. (Color) Snapshots of the flow after perturbing it from the oblique wave state (top left) to an upstream steady shock state (bottom right) due to an upstream avalanche of polystyrene beads (just inserted in the top middle frame). 1 s elapses between each frame. The density of the beads is about 900 kg/m^3, $F_0=3.07$, and $B_c=0.7$ indicated by a star in Fig. 6.

Finally, the supercritical oblique waves observed in the experiment appear to be influenced by other effects such as surface tension because the small-scale wave breaking in bores characterized by bubble inclusion was absent. Surprisingly, 2D hydraulic theory in conjunction with numerical simulations does match the 1D analysis well for supercritical shallow flows in the absence of bulk (turbulent) friction. Further (theoretical and numerical) research is required to include nonhydrostatic effects due to the combined actions of (averaged) two- and three-dimensional effects such as turbulence and surface tension.

ACKNOWLEDGMENTS

We gratefully acknowledge the Geophysical Fluid Dynamics (GFD) programs of 2005 and 2007 at the Woods Hole Oceanographic Institution for providing funding and facilities for this research. In particular, we thank O. Bühler and C. Doering, and C. Cenedese and J. Whitehead for providing a stimulating environment for many new ideas. We would also like to thank Keith Bradley for the design and construction of the experimental apparatus. In addition, we acknowledge Jack Whitehead, Sander Rhebergen, Larry

TABLE II. The experimental data for oblique shocks are presented: depth h_0 near the sluice gate and h_1 after the oblique shocks with ratio $H_1=h_1/h_0$, $L_s=\sqrt{(L_x^2+L_y^2)}$ is the length of the paddle and L_y its farthest distance from the channel wall, B_c is the scaled width at the nozzle, θ_s is the observed shock angle, and the shape is either symmetric with two perspex pieces or asymmetric with only one piece forming the contraction.

h_0	h_1	H_1	F_0	L_s	L_y	B_c	$\theta_s \pm 2^o$	Wedge shape
1.3	2.5	1.9231	2.79	30.5	5	0.75	26.7	Asymmetric
1.3	2	1.5385	2.94	30.5	1.9	0.81	26.7	Symmetric
1.3	2.2	1.6923	3.13	30.5	5	0.75	27.1	Asymmetric
1.3	2	1.5385	3.23	30.5	1.9	0.81	21.6	Symmetric
1.3	2	1.5385	3.37	30.5	3	0.7	22.1	Symmetric
1.3	2.5	1.9231	3.47	30.5	4	0.8	25.4	Asymmetric
1.3	2.2	1.6923	3.56	30.5	5	0.75	20.1	Asymmetric
1.3	2.3	1.7692	3.65	30.5	3	0.7	25.2	Symmetric

Pratt, and Joseph Keller for valuable discussions and Bert Vreman for proofreading. O.B. was partly funded through a fellowship of The Royal Netherlands Academy of Arts and Sciences.

APPENDIX A: OBLIQUE-WAVE DATA

We have tabulated the measurement data for the oblique jumps, used in Fig. 13, in Table II.

APPENDIX B: STABILITY

Stability of the steady solution in the reservoir is investigated by consideration of an approximate time dependent solution. This approximate solution consists of a moving shock in the reservoir starting in the neighborhood of the steady shock. It satisfies the following conditions. Upstream of the shock, the flow is supercritical and is therefore the same as the steady solution. The location of the shock will move in time, however. Downstream of the shock, the solution is subcritical and set in part by the criticality condition at the nozzle. The dynamics of the moving shock implies that the flow downstream of the shock is time dependent. The simplifying assumption is that the flow there is assumed to be quasistatic. It implies that explicit variations in time are ignored except to obtain the speed of the shock. We assume an instantaneous adjustment of the downstream flow to the slow movement of the shock, which in reality will be a fast but finite time process.

The above-mentioned solution can, in principle, be analyzed by solving the shock relations, mass continuity, and the Bernoulli relations up- and downstream of the shock, coupled to the criticality condition at the nozzle. Linear stability can be investigated after linearizing the system around the steady shock solution. A system of seven equations for eight variables results. A relation between the shock speed and the geometry then establishes whether the shock moves back to its original steady-state location, in the stable case, or not, in the unstable case.

Under the quasistatic assumption, only the reduced system of five equations is

$$u_1 h_1 b_1 = 1 = u_0 h_0 b_0, \tag{B1a}$$

$$h_1(u_1+s) = h_2(u_2+s), \tag{B1b}$$

$$h_1(u_1+s)^2 + \tfrac{1}{2}h_1^2/F_0^2 = h_2(u_2+s)^2 + \tfrac{1}{2}h_2^2/F_0^2, \tag{B1c}$$

$$u_1^2/2 + h_1/F_0^2 = 1/2 + 1/F_0^2, \tag{B1d}$$

$$u_2^2/2 + h_2/F_0^2 = \frac{1}{2}u_c^2 + h_c/F_0^2 = \frac{3}{2F_0^2}(u_2 h_2 F_0 b_1/b_c)^{2/3}, \tag{B1e}$$

where we have immediately used mass continuity and criticality at the nozzle to eliminate h_c and u_c,

$$u_c^2 = h_c/F_0^2, \quad u_c h_c b_c = u_2 h_2 b_1 \rightarrow h_c = (u_2 h_2 F_0 b_1/b_c)^{2/3}. \tag{B1f}$$

The six remaining unknowns in Eq. (B1a)–(B1f) are u_1, h_1, u_2, h_2, s, and b_1. In contrast, Ref. 5 also uses a linearization of Eqs. (B1a)–(B1d) and the relation

$$u_2^2/2 + h_2/F_0^2 = \tfrac{1}{2}u_c^2 + h_c/F_0^2 = \tfrac{3}{2}h_c/F_0^2, \tag{B2}$$

for fixed steady-state value h_c, instead of Eq. (B1c).

By combining and rewriting Eqs. (B1a), (B1d), (B1c), (B1b), (B1c), and (B1b), we find the following four equations:

$$(F_1 b_1/F_0)^{2/3} = (2+F_1^2)/(2+F_0^2), \tag{B3a}$$

$$z(2+F_2^2) = 3(F_2 b_1/b_c)^{2/3} z, \tag{B3b}$$

$$z^2 + z - 2(F_1+S_1)^2 = 0, \tag{B3c}$$

$$F_1 + S_1 = z(F_2\sqrt{z} + S_1), \tag{B3d}$$

for the remaining five variables,

$$F_1 = u_1 F_0/\sqrt{h_1}, \quad F_2 = u_2 F_0/\sqrt{h_2}, \quad z = h_2/h_1, \quad S_1 = sF_0/\sqrt{h_1}, \quad b_1. \tag{B4}$$

The next step is to linearize Eq. (B3) around $\bar{F}_1$, $\bar{F}_2$, $\bar{b}_1$, $\bar{z}$, and $S_1=0$. We then find

$$\frac{b_1'}{\bar{b}_1} = \frac{2(\bar{F}_1^2-1)}{(2+\bar{F}_1^2)}\frac{F_1'}{\bar{F}_1}, \tag{B5a}$$

$$\frac{b_1'}{\bar{b}_1} = \frac{2(\bar{F}_2^2 - 1)}{(2 + \bar{F}_2^2)} \frac{F_2'}{\bar{F}_2}, \tag{B5b}$$

$$(2\bar{z} + 1)z' = 4\bar{F}_1(F_1' + S_1), \tag{B5c}$$

$$\frac{F_1'}{\bar{F}_1} = (\bar{z} - 1)\frac{S_1}{\bar{F}_1} + \frac{F_2'}{\bar{F}_2} + \frac{3}{2}\frac{z'}{\bar{z}}. \tag{B5d}$$

Note from (B3) that $2\bar{F}_1^2 = \bar{z}(\bar{z}+1)$ and $\bar{F}_1 = \bar{z}^{3/2}\bar{F}_2$. After some algebra, one finds

$$3\bar{z}\left[\frac{(2\bar{z}+1)(\bar{F}_1^2 - \bar{F}_2^2)}{(2+\bar{F}_1^2)(1-\bar{F}_2^2)} - (\bar{z}+1)\right]\frac{b_1'}{\bar{b}_1}$$
$$= 2\frac{(\bar{F}_1^2 - 1)}{(2+\bar{F}_1^2)}[\bar{z}(2\bar{z}+1)(\bar{z}-1) + 6\bar{F}_1^2]\frac{S_1}{\bar{F}_1}. \tag{B6}$$

The signs of the terms on the right-hand side are positive since $\bar{F}_1 > 1$, $\bar{z} > 1$. The sign of the term on the left-hand side is investigated graphically; it is always a positive function of $\bar{F}_1^2 > 1$, once we have substituted the steady-state relations. Hence, when $S_1 > 0$, then $b_1' > 0$ and vice versa; the implication is that the steady shock is linearly unstable in the absence of additional bulk friction. We conclude that the extra assumption used in Ref. 5 and Eq. (21) was unnecessary, yet the result of our extended analysis is the same.

[1] A. W. Vreman, M. Al-Tarazi, J. A. M. Kuipers, M. van Sint Annaland, and O. Bokhove, "Supercritical shallow granular flow through a contraction: Experiment, theory and simulation," J. Fluid Mech. **578**, 233 (2007).

[2] J. M. N. T. Gray, Y.-C. Tai, and S. Noelle, "Shock waves, dead zones and particle-free regions in rapid granular free-surface flows," J. Fluid Mech. **491**, 161 (2003).

[3] O. Pouliquen and Y. Forterre, "Friction law for dense granular flows: Application to the motion of a mass down a rough inclined plane," J. Fluid Mech. **453**, 133 (2002).

[4] K. M. Hákonardóttir and A. J. Hogg, "Oblique shocks in rapid granular flows," Phys. Fluids **17**, 077101 (2005).

[5] P. Baines and J. Whitehead, "On multiple states in single layer flow," Phys. Fluids **15**, 298 (2003).

[6] P. G. Baines and P. A. Davies, "Laboratory studies of topographic effects in rotating and/or stratified fluids," in *Orographic Effects in Planetary Flows*, World Meteorological Organization GARP Publication No. 23 (World Meteorological Organization, Geneva, 1980), Chap. 8, pp. 233–299.

[7] A. T. Ippen and J. H. Dawson, "Design of channel contractions," Trans. ASCE **116**, 268 (1951).

[8] A. Shapiro, *The Dynamics and Thermodynamics of Compressible Fluid Flow* (Ronald, New York, 1954).

[9] D. D. Houghton and A. Kasahara, "Nonlinear shallow fluid flow over and isolated ridge," Commun. Pure Appl. Math. **21**, 1 (1968).

[10] P. Baines, *Topographic Effects in Stratified Flows* (Cambridge University Press, Cambridge, 1995).

[11] B. Akers, "Shallow water flow through a contraction," in Proceedings of the Geophysical Fluid Dynamics Fellowship Program, 2005, pp. 97–117, available online at http://www.whoi.edu/page.do?pid=12955.

[12] A. Defina and F. M. Susin, "Multiple states in open channel flow," in *Vorticity and Turbulence Effects in Fluid Structures Interactions*, Advances in Fluid Mechanics, edited by M. Brocchini and F. Trivellato (Wessex Institute of Technology Press, Southampton, UK, 2006), pp. 105–130.

[13] L. J. Pratt, "Hydraulic control of sill flow with bottom friction," J. Phys. Oceanogr. **16**, 1970 (1986).

[14] J.-M. Vanden-Broeck and J. B. Keller, "Weir flows," J. Fluid Mech. **176**, 283 (1987).

[15] D. F. Young, B. R. Munson, and T. H. Okiishi, *A Brief Introduction to Fluid Mechanics* (Wiley, New York, 1997).

[16] O. Bokhove, "Flooding and drying in discontinuous Galerkin finite element discretizations of shallow-water equations. Part 1: One dimension in ISI," J. Sci. Comput. **22**, 47 (2005).

[17] V. R. Ambati and O. Bokhove, "Space-time finite element shallow water flows," J. Comput. Appl. Math. **204**, 452 (2007).

[18] P. A. Tassi, O. Bokhove, and C. Vionnet, "Space discontinuous Galerkin method for shallow water flows—kinetic and hllc flux, and potential vorticity generation," Adv. Water Resour. **30**, 998 (2007).

[19] V. R. Ambati and O. Bokhove, "Space-time discontinuous Galerkin discretization of rotating shallow water equations," J. Comput. Phys. **225**, 1233 (2007).

[20] K. V. Karelsky and A. S. Petrosyan, "Particular solutions and Riemann problem for modified shallow water equations," Fluid Dyn. Res. **38**, 339 (2006).

[21] J. G. Esler, O. J. Rump, and E. R. Johnson, "Steady rotating flows over a ridge," Phys. Fluids **17**, 116601 (2005).

[22] E. B. Pitman and L. Le, "A two-fluid model for avalanche and debris flows," Proc. R. Soc. London, Ser. A **363**, 1573 (2005).